Article

Investigation of the Dominant Effects of Non-Spherical Particles on Particle–Wall Collisions

Zhoutao Cen [1], Yuxin Wu [1,*], Jingyu Wang [1], Jie Liu [1,2], Minmin Zhou [3], Shukuan Chen [4] and Dongqiang Zhao [4]

[1] Key Laboratory for Thermal Science and Power Engineering of Ministry of Education, Department of Energy and Power Engineering, Tsinghua University, Beijing 100084, China; cenzt22@mails.tsinghua.edu.cn (Z.C.)
[2] School of Safety Engineering, China University of Mining and Technology, Xuzhou 221116, China
[3] Key Laboratory of Energy Thermal Conversion and Control, Ministry of Education, School of Energy and Environment, Southeast University, Nanjing 210096, China
[4] Yan'an Thermal Power Plant, Datang Shaanxi Generation Co., Ltd., Yan'an 716004, China
* Correspondence: wuyx09@mail.tsinghua.edu.cn; Tel.: +86-10-62799641

Abstract: A deep understanding of the particle–wall collision (PWC) behaviors of non-spherical particles is important for managing gas–solid flows in industrial applications. It is important to identify the dominant parameters and to develop the common PWC prediction models for typical non-spherical particles. In this paper, different types of non-spherical particles were used to conduct the fundamental experiments. The effects of key parameters such as particle size, non-sphericity, wall roughness, and impact angle were analyzed. The results show that the trends of the collision coefficients with the impact angle for all non-spherical particles are similar. The dominant factors of particle–wall collisions are particle sphericity and wall roughness. A model with four parameters was fitted from the experimental data. The model can predict the collisions of non-spherical particles on rough steel walls with sizes ranging from 50 to 550 microns.

Keywords: particle–wall collision; non-spherical particles; restitution coefficient; friction coefficient

1. Introduction

The particle–wall collision phenomena have an important impact on the behavior of gas–solid two-phase flows, which are frequently found in energy, mechanical, and other industrial applications. For instance, solid fuel particles are generated in pulverizers to provide suitable particles for the coal powder furnace. More than 70% of the fine particles are smaller than about 74 μm, as coarse particles lead to slagging and incomplete combustion [1,2]. In typical types of particle classifiers such as cyclones, which are commonly used in chemical engineering, particle–wall collisions occur frequently and affect the separation efficiency and consequently the fineness of the particle sizes and instrument efficiency [3,4]. Therefore, it is important to understand the particle–wall collision behaviors of these types of particles, for better design of pulverizers, classifiers, and cyclones. Computational fluid dynamics (CFD) is an effective tool for the analysis of gas–solid two-phase flows. In order to produce accurate CFD simulations of such flows with wall interactions, particle–wall collision models are needed to predict the particle motions correctly. A model derived from impulsive equations and Coulomb's friction law is commonly used [5]. It describes the motion with the restitution coefficient *e*, which is related to the energy changes by plastic deformation, and the friction coefficient *f*, which represents the relative amount of friction force. These coefficients are not material properties and can be affected by many parameters such as the particle diameter and shape, the impact angle, the impact velocity, and the wall roughness. To apply the model in simulations, reasonable values of the coefficients must be provided.

Many experimental studies have been carried out on particle–wall collisions to analyze the impact behavior and to obtain the collision coefficients. For normal collisions with the

impact angle $\alpha_1 = 90°$, the friction coefficient f has no effect, while the restitution coefficient e is often expressed as a function of the impact velocity v_1 [6,7]. With v_1 increasing from the critical velocity, e increases from 0 to the maximum value as the adhesive effects decline relatively. Then, e starts to decrease with a very large v_1 as plastic deformation occurs [8]. For oblique collisions, both e and f generally have negative correlations with the impact angle α_1, which is the angle between the impact velocity direction and the wall [9–11]. If α_1 is sufficiently small, the particles may be able to gain a normal velocity component, causing e to increase over 1 [12]. Model equations of the collision coefficients based on α_1 have been proposed [13,14]. The relationships between e, f, and other conditions such as the particle diameter can also be found in previous studies [6,15–22].

For spherical and relatively large particles, constant collision coefficient values can offer a sufficient approximation to produce accurate predictions [5,23,24]. On the other hand, small non-spherical particles often exhibit irregular rebound behaviors [9]. The non-spherical shapes of the particles are known to alter the probabilities of different impact conditions on the local wall structure, leading to a smaller restitution coefficient e, and a larger friction coefficient f when the impact angle is small [25]. Additionally, many existing experimental studies have shown scattered results of e and f [26–30]. For non-spherical particles, the restitution coefficient's distribution is concentrated at small values. While the presence of a rough wall generally spreads the distribution of e, non-spherical particles' e is less affected by the wall roughness [25]. Therefore, these types of particles require more complex expressions of the collision coefficients, involving parameters that represent the shape factor, for accurate predictions of the rebound motions [31,32].

The particle velocities are often measured by optical methods, such as high-speed photography [18,33,34]. Particles that are easy to capture optically, such as glass beads, are commonly used in the experiments. On the other hand, typical non-spherical fuel particles such as coal and biomass have received less focus in existing studies. An experimental study by K.-P. Schade et al. investigated the impact behavior for coal particles and steel walls, focusing on the erosion effects [35]. Constant coefficient values and polynomial equations of the modified impact angles were provided, and the relations to the impact angle and velocity were shown. Experimental data of coke, polyethylene, and polystyrene particles reported by L. M. Gibson et al. [32]. revealed relations between the restitution coefficients and the rebound angles. Regression models involving the particle sphericity were proposed to describe the restitution coefficient components based on analysis of variance (ANOVA). More recently, M. Troiano et al. conducted experiments using coal, char, and ash particles with fixed impact angles, where the effects of impact velocities and carbon conversion degrees in cold and hot conditions were analyzed [36,37]. Rebound analyses have been successfully applied in the modeling of entrained-flow slagging gasifiers [38,39]. J. Xie et al. presented experimental results of using fly ash particles with a stainless-steel wall, and the effects of the impact velocity and angle on the rebound motion were reported [40]. R. Darko et al. presented the effects of an anisotropic virtual rough wall on the rebound motion [41]. W. Jacob et al. reported the importance of the particle shape for the rebound behavior [42]. However, the existing data for typical non-spherical particles are still limited. The collision behavior differences between those particles and regularly shaped particles have not been thoroughly analyzed.

Our previous work [25] analyzed and improved the virtual wall model for particle–wall collision, enabling it to better fit experimental results of spherical and non-spherical glass beads and glass powders colliding with steel walls. However, the real particles that have been widely used in real industrial applications vary in material and shape. In order to clarify the dominant effects on particle–wall collisions and to provide a model widely applicable to various types of non-spherical particles, the behaviors of typical non-spherical particles such as glass powder, coal, and biomass particles' collisions with a polished/unpolished steel wall were studied experimentally through optical measurements. The effects of the key parameters on the collision coefficients, such as the particle material and non-sphericity, wall roughness, impaction velocity, particle size, and impact angle,

were analyzed. In particular, the effect of sphericity was investigated through a thorough experimental comparison among different particle shapes, including spherical glass beads, Shepherd's purse seed with a similar ellipsoid shape and narrow sphericity, and coal/glass powder/biomass particles with wide range of sphericities. The common behaviors of these non-spherical particles were clarified through data analysis since the particle parameters such as particle size, particle shape, and impact velocity vary significantly and are hard to measure for each particle in industrial applications. An impact model based on the statistical parameters of a group of particles is thus meaningful for real applications; therefore, for this experiment, we chose particles with a large span of statistical characteristics, which is the same as in the industrial applications, and the average parameter value, such as that for particle size or particle sphericity, was used as the parameter input. Data analysis was based on a large amount of experimental statistical data, and it was carried out to obtain statistical characteristics with industrial application value and to analyze their dominant effects. An empirical model was proposed based on the experimental data, which can be used for CFD simulations of two-phase flows involving typical non-spherical particles with the size range of 50 μm to 550 μm.

2. Experimental Facility

Particle–wall collision experiments were conducted using different types of particles, expanding on the previous works with only glass beads [25]. The setup of the experimental facility is shown in Figure 1. The gas cylinder releases pressurized nitrogen into the pipe, which passes through the sonic nozzle flow meter to the particle feeder. The particles are pushed into the flow continuously by the piston driven by a motor, and the speed of the motor can be adjusted to control the rate. During the experiments, a very small constant motor speed was used to ensure a dilute flow. The particle feeding rate was not measured quantitively as the particle–wall interactions were not dependent on it in the dilute flow. After accelerating in a thin pipe with a diameter of 2 mm, the gas–solid flow is conveyed into the collision section where a rotatable block is installed. One of the rotatable block's vertical faces is used as the target wall for particle collision. The impact angle was partially controlled by turning the block's axle horizontally in the bearing. The particle–wall collisions occurred in the horizontal plane, illuminated by a laser sheet generator, and the high-speed camera captured particle trajectories from the top of the section. The photos were then stored by the computer to obtain the particle motion data.
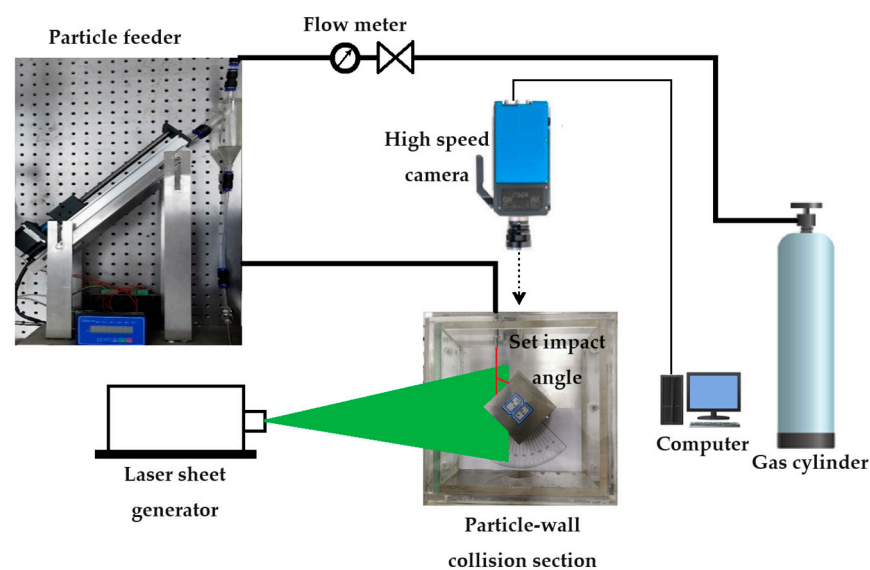

Figure 1. Schematic drawing of the experiment facility.

The resolution width of the high-speed camera (IDT NR3-S2, San Jose, FL, USA) was 256 pixels, and the frame rate was 4125 frames per second. For particles with diameter

d = 110 μm and velocity v = 6 m/s, the product of the resolution width and the frame rate was more than $19v/d$. As a result, with the pixel's physical size smaller than d, the image's physical width could be large enough to contain the rebound trajectories. The calibration factor was 62 um/pixel. The uncertainties that could lead to errors represented by pixels were related to the frame rate and the particle velocity. For example, given the frame rate of 4125 Hz and the particle velocity of 6 m/s, the velocity error caused by the pixels in this study was no more than 1.42%. The resolution height was adjusted for each case so that the entire particle trajectories were covered. The camera exposure was 117 μs, about half of the frame interval. The laser generator (GL 532-100HP) produced a continuous laser sheet of 20 mm×1 mm. Its wavelength was 532 nm and the power was 11 W. If the particle trajectory was out of the probe volume, it became invisible in the images and would be discarded during post-processing. Therefore, all the identified collisions occurred in the two-dimension plane, and the influence of three-dimensional rebound effects was relatively small. Given the frame rate of 4125 Hz and the particle velocity of 6 m/s, the velocity error caused by projecting three-dimensional motion onto a two-dimensional plane does not exceed 2.66%.

The photos captured of the particles (see Figure 2 for examples) were post-processed by a self-developed algorithm through a MATLAB program, as illustrated in Figure 3. The algorithm of the program was the same as that used in the previous work [25]. The wall boundary (Figure 3a) was located by applying a Hough transform. The particles' locations (Figure 3b) were found by subtracting the next image in the time sequence, applying a threshold, and then finding the connected components. There were usually multiple particles in one image, and we sought to correctly identify the same particle in successive images. For this purpose, it was assumed that the particle motion without collisions was almost uniformly linear, because the frame rate was high enough and the force effects would be ignored during the short period. The combinations of the particle locations in consecutive images were all tested; if a certain combination conformed with the assumption (forming a straight line with almost equal spacing), the locations would be matched and treated as the same particle. The resulting straight-line trajectories are shown in Figure 3c,d. Finally, particle–wall collisions were identified by matching the trajectories to and from the wall. An example of the post-processing result is shown in Figure 3e. The impact angle and impact velocity for each particle collision could then be identified through the post processing. The particles' velocity magnitudes and directions were derived from the post-processing results. For each collision instance, the data of the second to the fifth particles after collision and prior to collision were included. This was to avoid the strong reflective lights near the wall, and to keep the measured time small so that the assumption of uniformly linear motion held. With the drag force governed by Stokes' law, $F_d = 3\pi\mu d \cdot v$, the particle velocity relative to the flow v_r was proportional to $-dv_r/dt$, and v_r was subject to exponential decay with a very large time constant. For example, for glass particles with d = 160 μm, the time constant τ was 192 ms. Within the measurement time (3× frame time), the relative error of v_r was only $1 - \exp(-t/\tau) = 0.38\%$ [25]. The total error of the three types mentioned above was $1.42\% + 2.66\% + 0.38\% = 4.46\%$.

All of the experimental conditions are shown in Table 1. The target walls were unpolished and polished steel. The roughness levels *Ra* of the walls were 2.3 μm and 0.4 μm, respectively. Considering the widespread application of non-spherical particles, representative particles with a wide range of sphericity were selected, including two types of coal particles, one type of biomass particle, and glass powders. The sphericity is the ratio of the diameter of the equivalent circle of the two-dimensional projection area to the diameter of the smallest circle covering the projection. Since there was a significant difference in sphericity between non-spherical and spherical particles, Shepherd's purse seed with a more uniform sphericity was selected to fill the gap. The coal particle types had different Hardgrove Grindability Index (HGI) values; the majority of the cases involved Coal A with HGI = 50, while the softer Coal B with HGI = 91 was used in one case. In addition, the greater-hardness glass particles and lesser-hardness biomass particles were

involved to investigate the effect of hardness on particle collision. The particles were obtained by grinding the coal or biomass and then sieving them to different sizes. The diameters *d* listed in Table 1 were the median values of the measured size distributions in laser diffraction analysis. The carrier gas and the wall were at room temperature; as the effects of the temperature have been covered by previous studies, this work primarily focused on the particle non-sphericity instead.

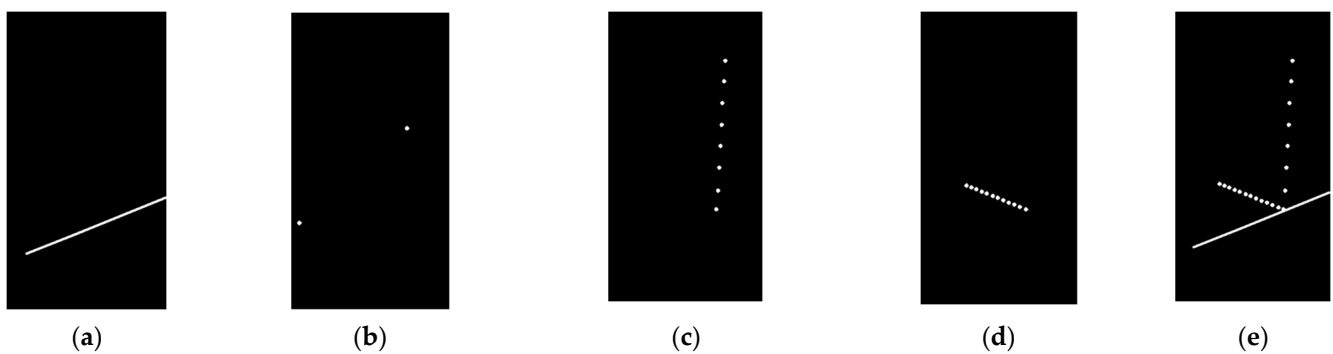**Figure 2.** Examples of the captured photos.

| (a) | (b) | (c) | (d) | (e) |

Figure 3. Illustration of the post-processing program. (**a**) Wall boundary through Hough transformation, (**b**) particle location through comparison of neighboring images, (**c**) particle trajectory prior to collision, (**d**) particle trajectory after collision, (**e**) complete data of a particle–wall collision instance.

Table 1. Experimental conditions.

No.	Particle	d (μm)	v_1 (m/s)	Sphericity	Target Wall	Identified Collisions
1~2	Coal A	110	3/9	0.69	Steel	
3	Coal A	110	6	0.69	Polished Steel	9867
4~6	Coal A	60/110/220	6	0.69	Steel	
7	Coal B	150	6	0.64	Steel	2154
8~9	Biomass	310/550	6	0.23	Steel	3556
10~12	Glass beads	85/130/165	6	~0.95	Steel	26,676
13~15	Glass beads	85/130/165	6	~0.95	Polished Steel	
16~17	Glass powder	165/205	6	~0.75	Steel	8605
18~19	Glass powder	165/205	6	~0.75	Polished Steel	
20	Shepherd's purse seed	500	6	0.78	Steel	1441

At the outlet of the acceleration pipe, the particles' actual velocities and angles varied from the gas velocity and the injection angle, and the exact values could not be controlled individually. Therefore, the results were regrouped by the measured velocity and angle to analyze the collisions statistically [25]. In Table 1, the median impact velocities v_1 of the conditions are listed. For each case, the experiments were repeated with different injection angles, and the measured impact angles were regrouped into 20°, 30°, 40°, 50°, 60°, and 70°. These conditions were designed to analyze the wall collision characteristics of the non-spherical particles, as well as the effects of wall roughness, impact velocity, particle size, and particle hardness. Figure 4 shows different particles. The detailed conditions are listed in Table 1; the data set included 52,299 valid collisions for all experimental cases.
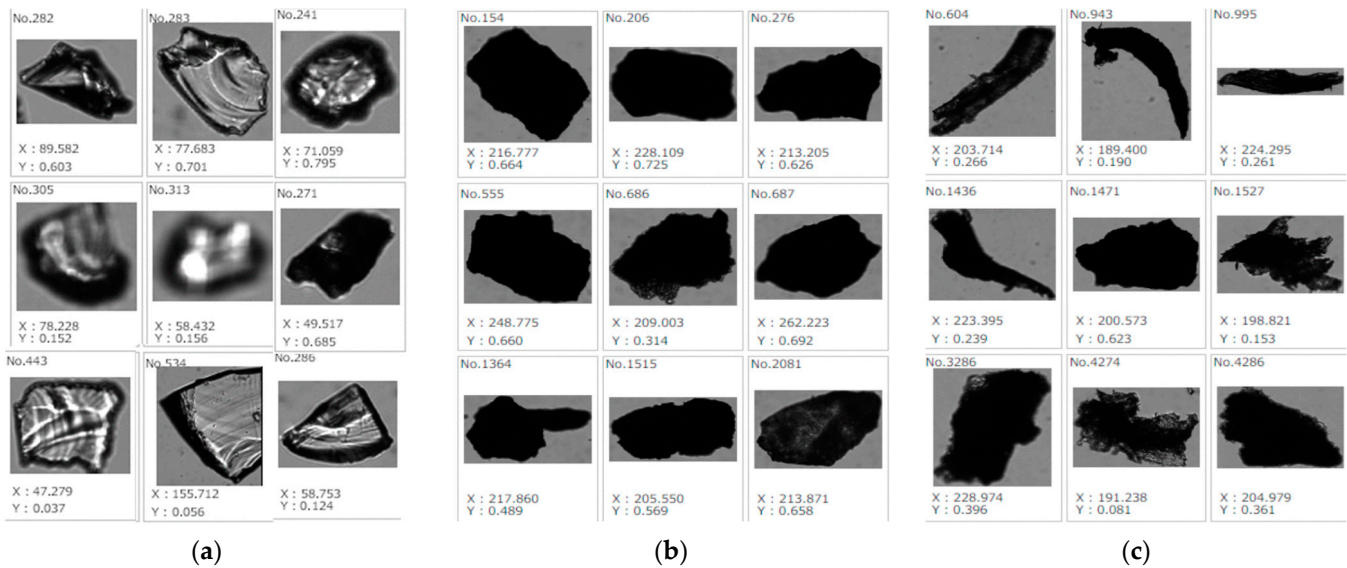

Figure 4. Images of different particles. (**a**) Glass powder, (**b**) coal powder, (**c**) biomass.

3. Results and Discussion

3.1. Effects of Key Parameters on Particle Collision

The results for the particle velocities were analyzed by applying the model with the restitution coefficient e and the friction coefficient f. These coefficients were calculated as [5,25]

$$e = v_{2n}/v_{1n} \tag{1}$$

$$f = \frac{v_{1t} - v_{2t}}{(1+e)v_{1n}} \tag{2}$$

where v_{1n} and v_{1t} are the normal and tangential impact velocities, and v_{2n} and v_{2t} are the normal and tangential rebound velocities. Similar to the non-spherical glass particles, the rebound motions of the non-spherical particles with different materials and shapes were scattered with large variance. The data were filtered by an outlier detection algorithm based on the interquartile range IQR. The values outside $[Q_L - 1.5\,\mathrm{IQR}, Q_U + 1.5\,\mathrm{IQR}]$ were excluded, where Q_L and Q_U are the lower and upper quartiles of the results data [43]. In the experiment, the impact angles were regrouped and it was difficult to accurately control the impact velocity, so the filtered data were analyzed statistically, to produce results revealing the statistical collision behaviors, with use in real industrial applications.

Figure 5 shows the mean values of e and f for the coal particles colliding with the steel wall, with different impact angles α_1. The impact velocities of the cases are in the 6 m/s group unless otherwise noted. The dependencies of e and f on α_1 of the coal particles follow the same patterns as for the glass particles; e decreases with decreasing slopes when α_1 becomes larger, and f decreases with increasing α_1 approximately linearly. For the coal A particles with HGI = 50, both e and f are almost the same as those of the non-spherical glass

particles with the steel wall. Unlike the glass particles, the coal A particles with different diameters have similar values of collision coefficients. Although glass and coal have distinct material properties, their rebound motions on rough walls can be very similar due to their irregular particle shapes. For the softer coal B particles with HGI = 91, e is larger than coal A for medium to large impact angles $\alpha_1 \geq 40°$, while f has the same value as coal A. There are complex relationships between the HGI and the particles' mechanical properties such as the compressive ductility and the ultimate stress [44,45], and it is unknown which property contributes most to the different behaviors during collision. However, such differences are smaller than the differences caused by the particle sphericity.
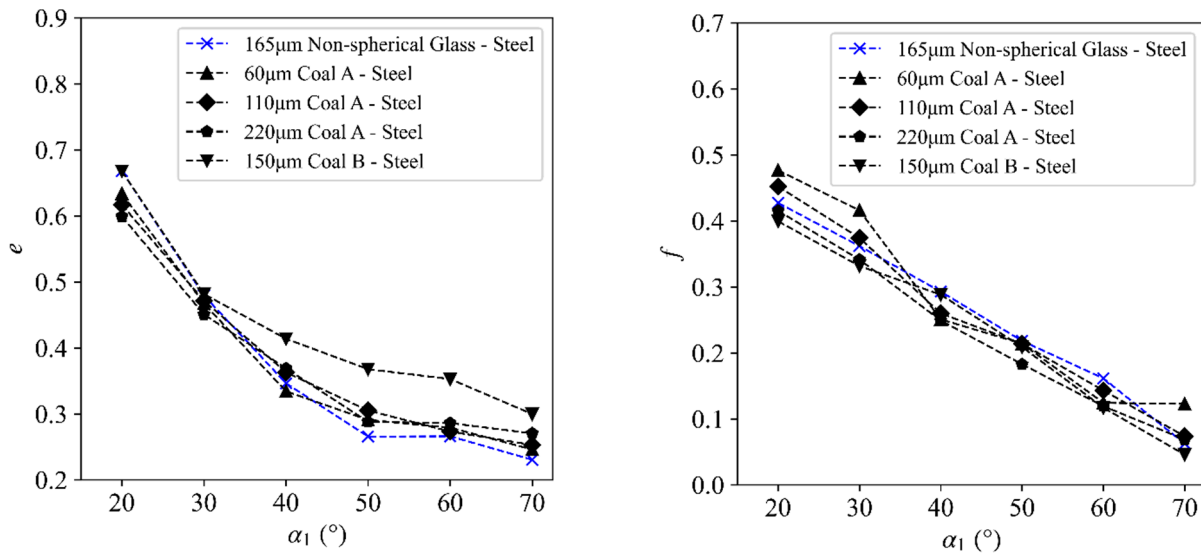

Figure 5. Collision coefficients of coal particles with steel wall.

The effects of the impact velocity on the collision coefficients are shown in Figure 6. Coal A particles and the steel wall were used in these cases. With the impact velocity increasing, small decreases in e and increases in f were observed. The results were consistent with the existing theories about velocity's effects at slow speeds [6]. And the effects of collision velocity were limited, too.
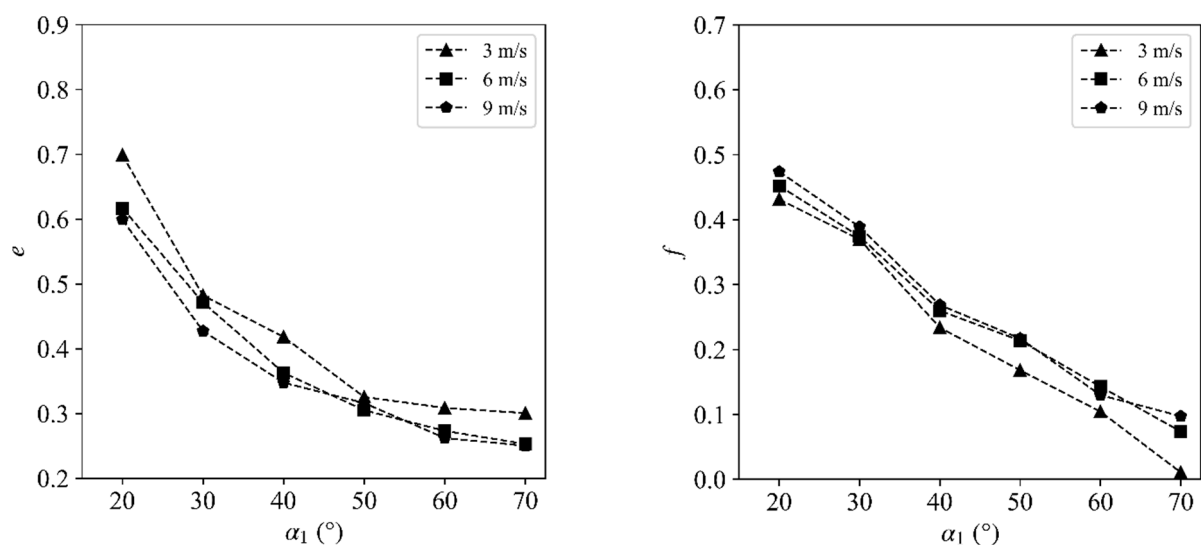

Figure 6. Effects of the impact velocity on the collision coefficients.

Figure 7 shows the results of the coal A particles with the steel wall and the polished steel wall. For the polished wall with lower roughness, the dependence of e on the impact

angle α_1 was smaller, and e became smaller than that for the rough wall with a small α_1. This was caused by the particles' direction changes for glancing impacts; for coal A particles ($d = 110$ μm) within the $\alpha_1 = 20°$ group, the mean rebound angle with the rough steel wall was 5° larger than that with the polished steel wall. These effects are often attributed to the rough wall's local inclinations [9,10]. The coal particles' e can be as low as 0.45 with $\alpha_1 \rightarrow$ 20° when colliding with the polished wall, which is lower than that of the non-spherical glass particles. On the other hand, the f of coal particles has little difference from that of the non-spherical glass particles, and both cases have lower f values than when colliding with the rough wall, when α_1 is small.
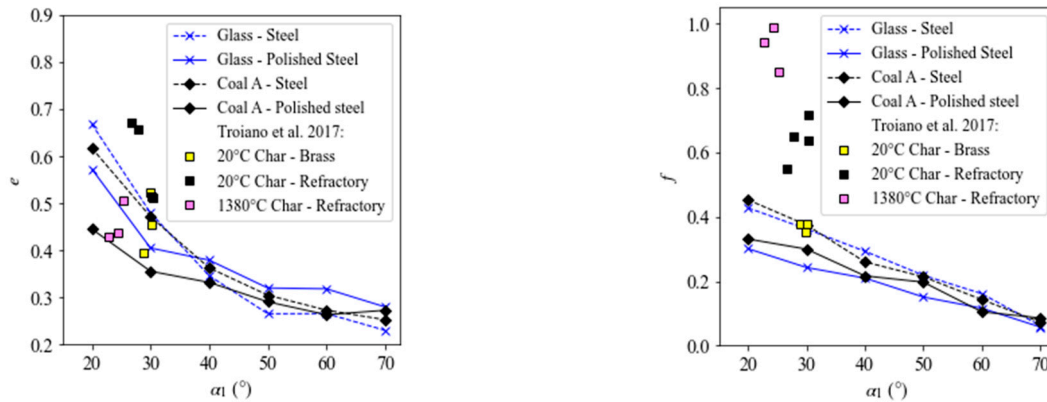

Figure 7. Effects of the wall roughness and the temperature on the collision coefficients (compared with the results in Troiano et al., 2017 [36]).

For applications of fuel particles such as thermal power generation, the effects of the temperature are important for the particle–wall collision behaviors. To analyze such effects, the collision coefficients of the coal particles were compared with the results in Troiano et al., 2017 [36] (Figure 7). At room temperature, the cited case with the brass wall resulted in the same collision coefficients as the steel wall in this paper, due to the similar wall material types. The refractory wall had much greater roughness so its friction coefficient f was larger. As the temperature rose to 1380 °C, the refractory wall's f became even larger as the particles' tangential rebound velocities decreased [36].

There are few existing studies about thermal effects on particle–wall collision [36,37,46]. Dong et al. 2014 [46] showed that when there are temperature gradients between the inlet and the wall, the effects of the thermophoretic force are important for the wall collisions of small ($d = 20$ μm) SiO_2 particles. In this paper, the coal particle's size was much larger, reducing the influences of external forces. Troiano et al. 2017 [36] showed that collision behavior changes under hot conditions with char/slag transition, which can be explained by changes in mechanical properties. For example, ash particles' rebound velocities decrease at high temperatures, as the particle stickiness increases significantly [47]. But the results in Figure 7 show that temperature has limited effects on particle collision if the mechanical properties of the particle do not have an apparent change. Especially for non-spherical particles, even with material changes (e.g., from coal to char), the particle wall behaviors for a similar wall roughness show great similarities. The results in Figure 7 also show that wall roughness has an apparent effect on the friction coefficient.

We take the biomass particle–steel wall collision data with different particle sizes as an example, as shown in Figure 8. Similar to the case with coal A particles, the collision coefficients of these biomass particles are close to those of the non-spherical glass particles with the rough steel wall. The results prove that changing the particle diameter causes only small variations in e for large impact angles, and it has nearly no effect on f for non-spherical particles with low sphericity.
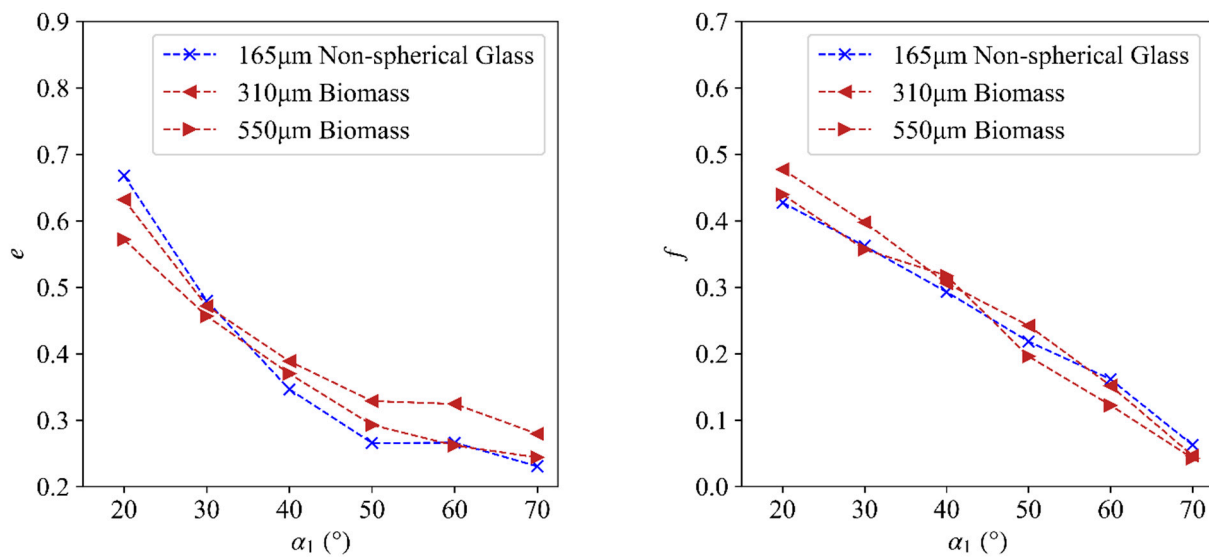
Figure 8. Collision coefficients of biomass particles with steel wall.

3.2. Similarities of the Non-Spherical Particle Collisions

For a thorough comparison among the different particle types, Figures 9 and 10 show the collision coefficients of all the cases. In Figure 9a, the restitution coefficients of the spherical glass particles have significantly different values and trends from those of the non-spherical particles. With large impact angles α_1, the e of glass beads can be up to 0.6~0.8, while all the non-spherical particles have much lower e results, ranging from 0.2 to 0.4. Specifically, the restitution coefficients for non-spherical particles of coal, glass powder, and biomass impacting with unpolished steel are shown as the shaded region in Figure 9a; it is interesting that the region is concentrated, although the materials are very different, as well as the particle size and particle sphericity. Meanwhile, these regions for the restitution coefficients of coal and glass powder impacting with polished steel are more scattered than that for steel cases. This difference shows that sphericity and wall roughness have more important effects on particle wall collision behaviors compared to the other collision parameters. It can also be observed that the restitution coefficient of Shepherd's purse seed is larger than that of all other non-spherical particles, but is lower than those of most of the spherical particles. Based on these comparisons, it is clear that sphericity plays a dominant role in setting particle impaction behavior when it is less than 0.7, and that such an effect makes the particle behavior similar. Such a trend is shown clearly in Figure 9b with $\alpha_1 = 60°$, where the spherical glass particles' e is positively correlated with the particle diameter d. On the other hand, the coal and biomass particles' e values are close to a horizontal line at around 0.3 regardless of d. The results of the non-spherical particles with the unpolished steel wall are highlighted with shaded areas in both figures. The areas are also very small and concentrated.

The friction coefficients f as functions of α_1 and d are plotted in Figure 10a,b. As $f \to 0$ for normal collisions ($\alpha_1 = 90°$), the differences among the conditions become clear with small impact angles. With $\alpha_1 = 20°$, the glass beads' f is generally lower than those of the coal and biomass particles. Similar observations can be made based on Figure 10b concerning the correlations of f with d. The shaded areas containing the fuel particles' results with the steel wall have limited ranges. Therefore, it can be concluded that the particle non-sphericity and the wall roughness are the major influencing factors of collisions. In particular, the collisions between non-spherical particles and the rough steel wall behave similarly, and it is possible to develop a simple particle-collision model for a wide range of non-spherical particles with impaction angles ranging from 0 degrees to 90 degrees, sizes ranging from 50 μm to 550 μm, material HGI hardness values ranging from 50 to over 100, and collision velocities ranging from 3 m/s to 10 m/s or higher.
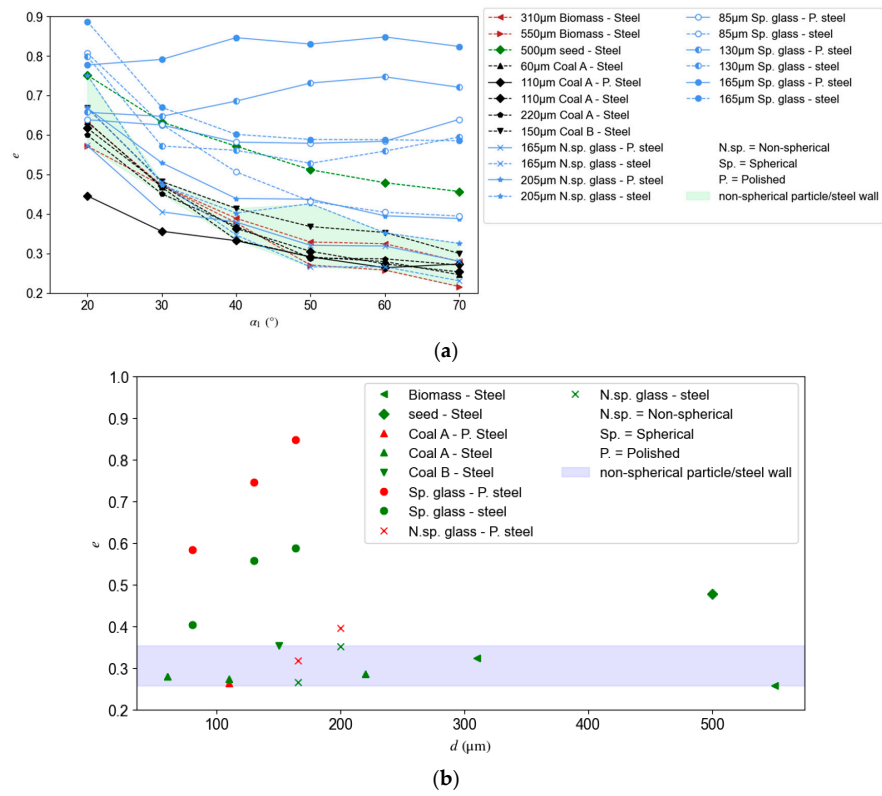
Figure 9. Comparison of restitution coefficients e (v_1 = 6 m/s), as functions of (**a**) impact angle α_1 and (**b**) particle diameter d with $\alpha_1 = 60°$.
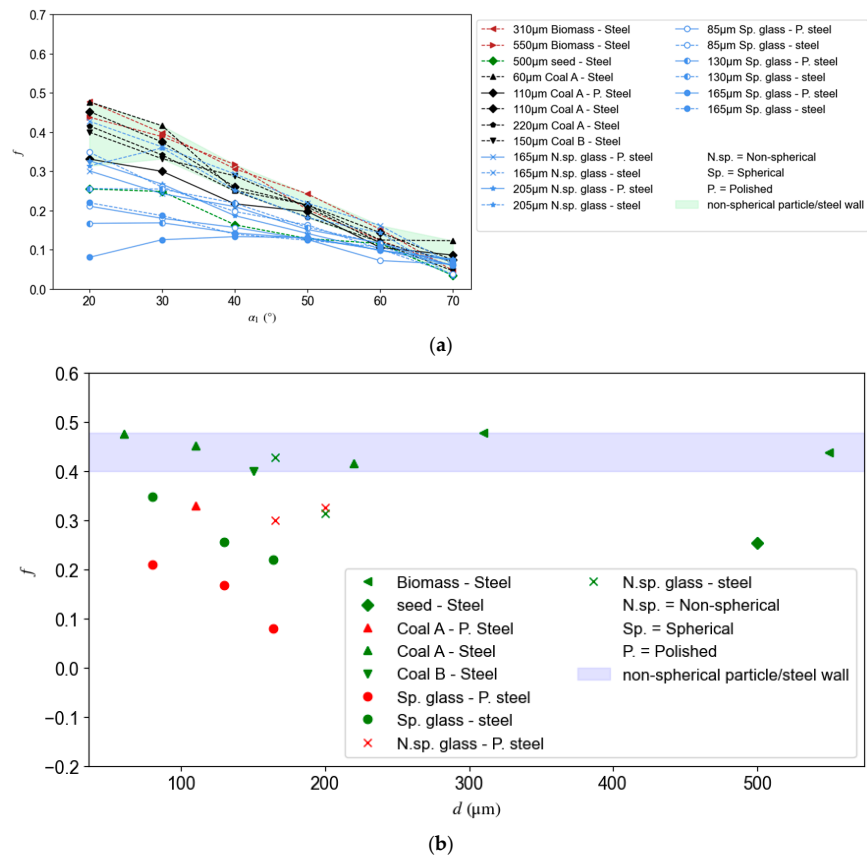

Figure 10. Comparison of friction coefficients f (v_1 = 6 m/s), as functions of (**a**) impact angle α_1 and (**b**) particle diameter d with $\alpha_1 = 20°$.

In order to directly show the effect of sphericity on both *e* and *f*, the restitution coefficients and the friction coefficients of different particle types as functions of sphericity under the fixed impact angle of 40° and impact velocity of 6 m/s are shown in Figure 11. It is clear that *e* decreases first when sphericity decreases from 1.0 to 0.75, and then *e* reaches a steady narrow range from 0.3 to 0.45 as sphericity decreases to very small values such as 0.23. On the contrary, *f* increases with the decrease in sphericity.
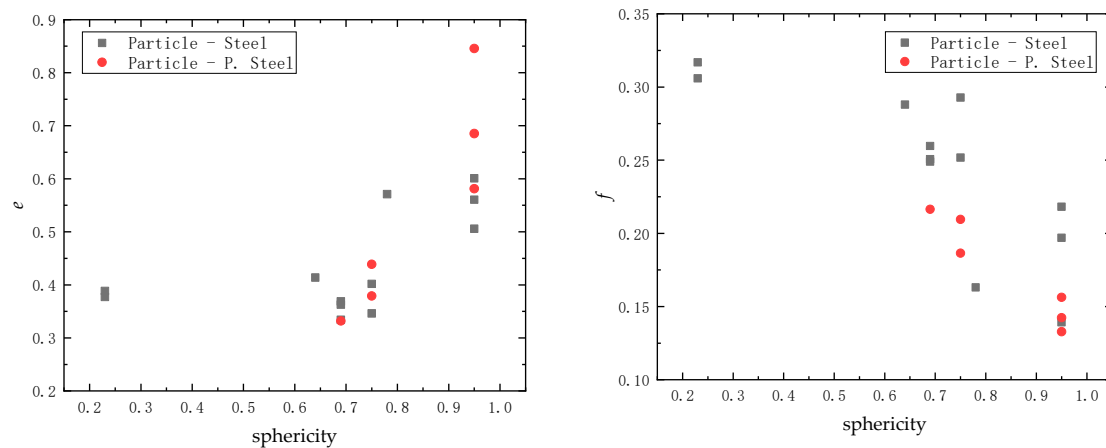

Figure 11. Restitution coefficients and friction coefficients as functions of sphericity given an impact angle of 40° and impact velocity of 6 m/s.

3.3. Modeling

The results show that all non-spherical particles exhibit similar stochastic behaviors during particle–wall collisions, and their rebound velocities and collision coefficients have wide distributions. Figure 12 shows the scatter plot of the velocity ratio $e_v = v_2/v_1$ for the coal A particles ($d = 110$ μm) with the steel wall. The value e_v is chosen instead of $e = v_{2n}/v_{1n}$ for model validation here, because e_v is still applicable with $\alpha_1 \to 0$ and $v_{1n} \to 0$ unlike *e*. With both a small α_1 (grazing impacts) and large α_1 (near-normal impacts), the distribution of e_v has large variations. To build a model for such collisions, it is necessary to introduce parameters representing the variations for both cases. Based on Wang's work [31], the model with four parameters is used here (modeled restitution coefficient e_m, standard deviation of the modeled restitution coefficient Δe_m, modeled friction coefficient f_m, standard deviation of the random wall angle $\Delta \gamma$). The subscript "m" of e_m and f_m is used to differentiate them from the apparent coefficients *e* and *f* based on the impaction angle without a consideration of wall roughness. The modeled restitution coefficient, e_m is assumed to follow a normal distribution $N(e_m, \Delta e_m^2)$, f_m is set to a constant f_m, and the collision plane is assumed to have an inclination angle $\gamma \sim N(0, \Delta \gamma^2)$ against the wall [31]. Given the four parameters e_m, Δe_m, f_m, and $\Delta \gamma$, the stochastic collision results are predicted as follows:

1. Generating random *e* and γ from the corresponding distributions;
2. Calculating the rebound velocity (v_{2n}, v_{2t}), based on the virtual wall with an inclination of γ against the apparent wall. The equations are [31]

$$v_{2n} = -e v_{1n} \tag{3}$$

$$v_{2t} = \begin{cases} (5v_{1t} + d\omega_1)/7, & \text{non-sliding} \\ v_{1t} - f(1+e)\varepsilon_0 v_{1n}, & \text{sliding} \end{cases} \tag{4}$$

where ω_1 is the impact angular velocity, and ε_0 is the sign function of the velocity direction of the contact surface. It should be noted that the non-sliding equation in (4) results in a different *f* from the provided f_m, and the presence of γ strongly affects the rebound behavior for glancing impacts. Therefore, although the model parameters

e_m and f_m are independent of α_1, the predicted e and f will depend on α_1, which is consistent with the experimental data.
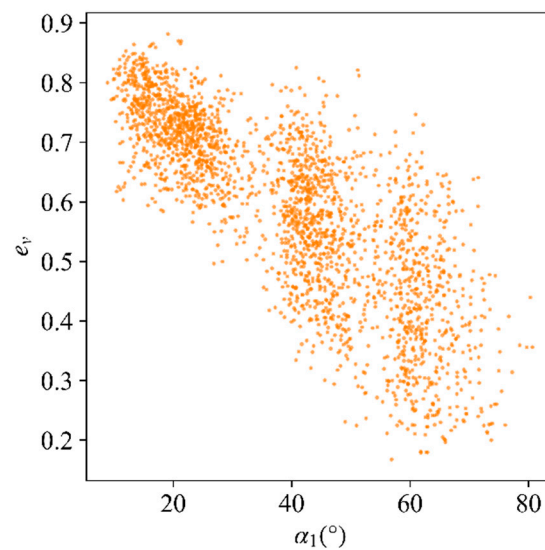

Figure 12. Scatter plot of e_v for coal A particles with steel wall.

The parameters e_m, Δe_m, f_m, and $\Delta \gamma$ are fitted from the experimental data, using the median and lower and upper quartiles of e_v and the rebound angle α_2, for each group of impact angle α_1. For the coal A particles with the steel wall, the results are shown in Table 2. The model's goodness of fit was evaluated by using the relative velocity distribution error R: [31]

$$\delta = \left(\frac{e_{v,modal}}{e_{v,data}} - 1 \right)^2 + \left(\alpha_{2,modal} - \alpha_{2,data} \right)^2 \tag{5}$$

$$R = \sqrt{\sum_{\alpha_1 = 20°,30°,...,90°} \delta_{\alpha_1,median} + \frac{\delta_{\alpha_1,25\%} + \delta_{\alpha_1,75\%}}{2}} \tag{6}$$

Table 2. Model parameters for fuel particles with steel wall based on Coal A data.

Particle Type	e_m	Δe_m	f_m	$\Delta \gamma$	Relative Error
Coal A	0.28	0.13	0.44	9.66	6.0%

This is composed of e_v's relative error and α_2's absolute error, as they both contributed to the rebound velocity's relative change. The distribution's median, lower quartile (25%), and upper quartile (75%) are all considered. The relative error R is 6.0% for the case in Table 2, making it possible to apply the model in the simulations.

Considering the similarity of the collision behaviors of all the non-spherical particles with the unpolished wall, it is expected that a single set of parameters in Table 2 can fit multiple conditions' results. Figure 13 compares the predicted e_v by the model with these parameters, and the experimental data of three different cases. When colliding with the rough steel wall, both the 110 μm coal A particles and the 310 μm biomass particles show good matches between the model and the data. Only slight deviations are observed for the 150 μm coal B particles. Nevertheless, e_v values of the coal A particles with the polished steel are larger and have narrower distributions for grazing impacts, deviating from the predictions of the same model parameters.
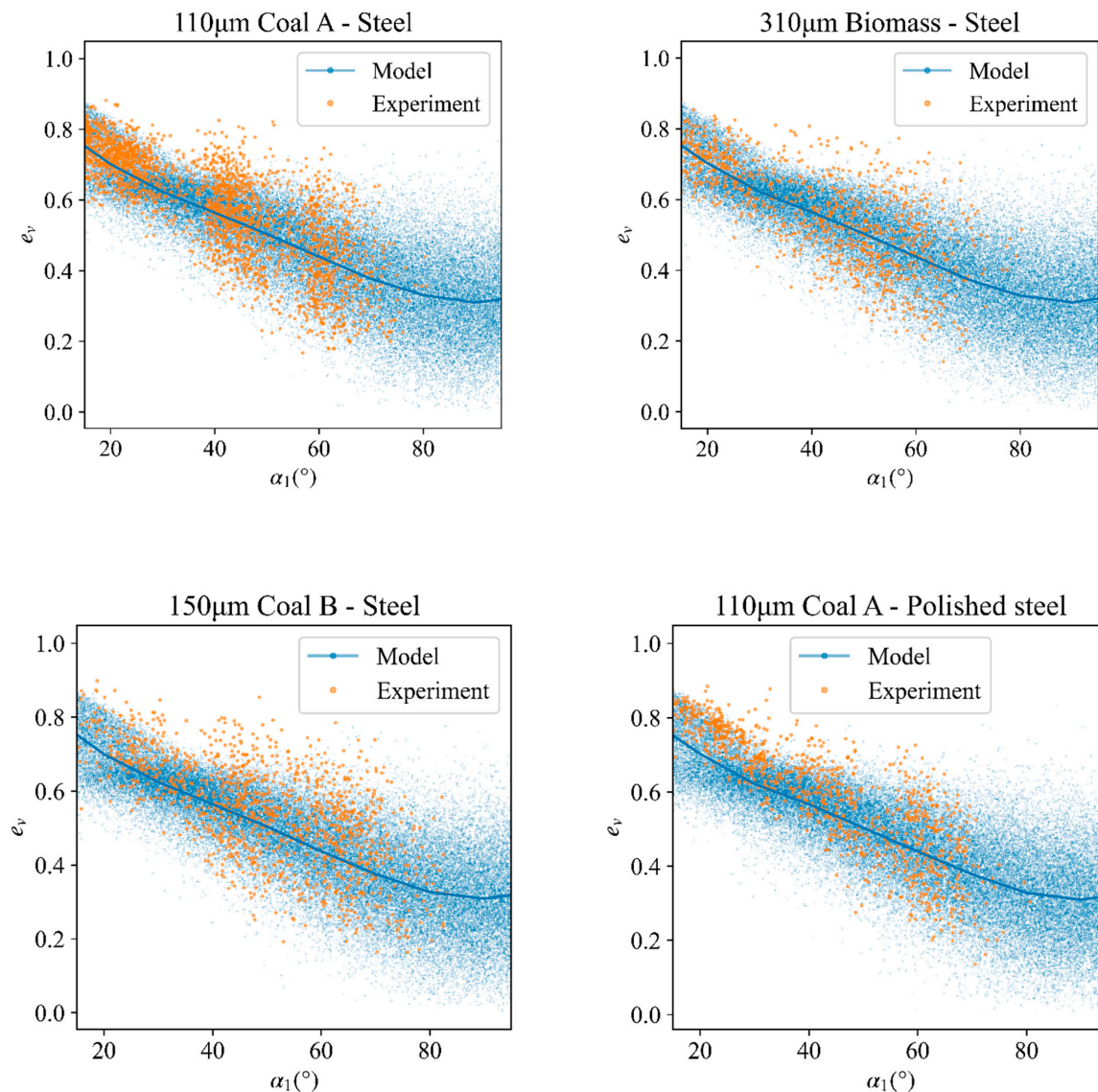
Figure 13. Comparisons of the model with the experimental data.

The results in Figure 13 indicate that this model can be applied to typical non-spherical particles impacting rough steel walls, which are frequently found in industrial uses. Even without experimental data for the specific particle–wall combination, the set of parameters in Table 2 can provide reasonable accuracy, as the collision behaviors mostly depend on the particle non-sphericity and the wall roughness. By sampling the model, it is possible to predict the non-spherical particles' rebound motions and improve CFD simulations of related gas–solid flows.

4. Conclusions

In this study, particle–wall collision experiments were carried out with typical non-spherical particles, including glass powders, coal, and biomass particles, colliding with polished and rough walls. The results of the collision coefficients were determined, and the effects of various parameters were analyzed. It has been concluded that

1. The dominating factors of particle–wall collisions are the particle non-sphericity and the wall roughness. Most of the cases with non-spherical particles and a rough steel wall show similar collision behaviors.
2. The effects of the particle diameter on the collision coefficients of non-spherical particles can be ignored, unlike for spherical particles.

3. It is possible to predict the particles' rebound motions for a wide range of typical non-spherical particles with a four-parameter model. Using the fitted values in Table 2, collisions of typical non-spherical particles with sizes ranging from 50 μm to 550 μm on steel walls can be predicted with reasonable accuracy.

References

1. Sarkar, D. *Thermal Power Plant: Design and Operation*; Elsevier: Amsterdam, The Netherlands, 2015.
2. Shah, K.V.; Vuthaluru, R.; Vuthaluru, H.B. CFD based investigations into optimization of coal pulveriser performance: Effect of classifier vane settings. *Fuel Process. Technol.* **2009**, *90*, 1135–1141. [CrossRef]
3. Ataş, S.; Tekir, U.; Paksoy, M.A.; çelik, A.; çam, M.; Sevgel, T. Numerical and experimental analysis of pulverized coal mill classifier performance in the Soma B Power Plant. *Fuel Process. Technol.* **2014**, *126*, 441–452. [CrossRef]
4. Wei, Q.; Sun, G.; Yang, J. A model for prediction of maximum-efficiency inlet velocity in a gas-solid cyclone separator. *Chem. Eng. Sci.* **2019**, *204*, 287–297. [CrossRef]
5. Tsuji, Y.; Oshima, T.; Morikawa, Y. Numerical Simulation of Pneumatic Conveying in a Horizontal Pipe. *KONA Powder Part. J.* **1985**, *3*, 38–51. [CrossRef]
6. Wall, S.; John, W.; Wang, H.; Goren, S.L. Measurements of Kinetic Energy Loss for Particles Impacting Surfaces. *Aerosol Sci. Technol.* **1990**, *12*, 926–946. [CrossRef]
7. Dunn, P.F.; Brach, R.M.; Caylor, M.J. Experiments on the Low-Velocity Impact of Microspheres with Planar Surfaces. *Aerosol Sci. Technol.* **1995**, *23*, 80–95. [CrossRef]
8. Thornton, C.; Ning, Z. A theoretical model for the stick/bounce behaviour of adhesive, elastic-plastic spheres. *Powder Technol.* **1998**, *99*, 154–162. [CrossRef]
9. Sommerfeld, M.; Huber, N. Experimental analysis and modelling of particle-wall collisions. *Int. J. Multiph. Flow* **1999**, *25*, 1457–1489. [CrossRef]
10. Konan, N.A.; Kannengieser, O.; Simonin, O. Stochastic modeling of the multiple rebound effects for particle–rough wall collisions. *Int. J. Multiph. Flow* **2009**, *35*, 933–945. [CrossRef]
11. Sondergaard, R.; Chaney, K.; Brennen, C.E. Measurements of Solid Spheres Bouncing Off Flat Plates. *J. Appl. Mech.* **1990**, *57*, 694–699. [CrossRef]
12. Brach, R.M.; Dunn, P.F.; Li, X. Experiments and Engineering Models of Microparticle Impact and Deposition. *J. Adhes.* **2000**, *74*, 227–282. [CrossRef]
13. García Pérez, M.; Vakkilainen, E.; Hyppänen, T. Unsteady CFD analysis of kraft recovery boiler fly-ash trajectories, sticking efficiencies and deposition rates with a mechanistic particle rebound-stick model. *Fuel* **2016**, *181*, 408–420. [CrossRef]
14. Stanton, D.W.; Rutland, C.J. *Modeling Fuel Film Formation and Wall Interaction in Diesel Engines*; SAE International: Warrendale, PA, USA, 1996.
15. Brilliantov. *Kinetic Theory of Granular Gases*; Oxford University Press: Oxford, UK, 2004.
16. Gorham, D.A.; Kharaz, A.H. The measurement of particle rebound characteristics. *Powder Technol.* **2000**, *112*, 193–202. [CrossRef]
17. Marinack, M.C.; Musgrave, R.E.; Higgs, C.F. Experimental Investigations on the Coefficient of Restitution of Single Particles. *Tribol. Trans.* **2013**, *56*, 572–580. [CrossRef]
18. Aryaei, A.; Hashemnia, K.; Jafarpur, K. Experimental and numerical study of ball size effect on restitution coefficient in low velocity impacts. *Int. J. Impact Eng.* **2010**, *37*, 1037–1044. [CrossRef]
19. Falcon, E.; Laroche, C.; Fauve, S.; Coste, C. Behavior of one inelastic ball bouncing repeatedly off the ground. *Eur. Phys. J. B—Condens. Matter Complex. Syst.* **1998**, *3*, 45–57. [CrossRef]
20. Tsai, C.; Pui, D.Y.H.; Liu, B.Y.H. Capture and Rebound of Small Particles Upon Impact with Solid Surfaces. *Aerosol Sci. Technol.* **1990**, *12*, 497–507. [CrossRef]

21. Kleinhans, U.; Wieland, C.; Frandsen, F.J.; Spliethoff, H. Ash formation and deposition in coal and biomass fired combustion systems: Progress and challenges in the field of ash particle sticking and rebound behavior. *Prog. Energ. Combust.* **2018**, *68*, 65–168. [CrossRef]

22. Chen, S.; Liu, W.; Li, S. A fast adhesive discrete element method for random packings of fine particles. *Chem. Eng. Sci.* **2019**, *193*, 336–345. [CrossRef]

23. Foerster, S.F.; Louge, M.Y.; Chang, H.; Allia, K. Measurements of the collision properties of small spheres. *Phys. Fluids* **1994**, *6*, 1108–1115. [CrossRef]

24. Kleis, I.; Hussainova, I. Investigation of particle—Wall impact process. *Wear* **1999**, *233*, 168–173. [CrossRef]

25. Wang, J.; Zhang, M.; Feng, L.; Yang, H.; Wu, Y.; Yue, G. The behaviors of particle-wall collision for non-spherical particles: Experimental investigation. *Powder Technol.* **2020**, *363*, 187–194. [CrossRef]

26. Tabakoff, W.; Malak, M.F. Laser Measurements of Fly Ash Rebound Parameters for Use in Trajectory Calculations. *J. Turbomach.* **1987**, *109*, 535–540. [CrossRef]

27. Grant, G.; Tabakoff, W. Erosion Prediction in Turbomachinery Resulting from Environmental Solid Particles. *J. Aircraft.* **1975**, *12*, 471–478. [CrossRef]

28. Montaine, M.; Heckel, M.; Kruelle, C.; Schwager, T.; Pöschel, T. Coefficient of restitution as a fluctuating quantity. *Phys. Rev. E* **2011**, *84*, 41306. [CrossRef] [PubMed]

29. van Beek, M.C.; Rindt, C.C.M.; Wijers, J.G.; van Steenhoven, A.A. Rebound characteristics for 50-μm particles impacting a powdery deposit. *Powder Technol.* **2006**, *165*, 53–64. [CrossRef]

30. Hastie, D.B. Experimental measurement of the coefficient of restitution of irregular shaped particles impacting on horizontal surfaces. *Chem. Eng. Sci.* **2013**, *101*, 828–836. [CrossRef]

31. Wang, J.; Yang, H.; Feng, L.; Zhang, M.; Wu, Y.; Yue, G. The behaviors of particle-wall collision for non-spherical particles: Modeling analysis. *Powder Technol.* **2020**, *366*, 137–143. [CrossRef]

32. Gibson, L.M.; Gopalan, B.; Pisupati, S.V.; Shadle, L.J. Image analysis measurements of particle coefficient of restitution for coal gasification applications. *Powder Technol.* **2013**, *247*, 30–43. [CrossRef]

33. Gondret, P.; Lance, M.; Petit, L. Bouncing motion of spherical particles in fluids. *Phys. Fluids* **2002**, *14*, 643–652. [CrossRef]

34. Antonyuk, S.; Heinrich, S.; Tomas, J.; Deen, N.G.; van Buijtenen, M.S.; Kuipers, J.A.M. Energy absorption during compression and impact of dry elastic-plastic spherical granules. *Granul. Matter.* **2010**, *12*, 15–47. [CrossRef]

35. Schade, K.P.; Erdmann, H.J.; Hädrich, T.; Schneider, H.; Frank, T.; Bernert, K. Experimental and numerical investigation of particle erosion caused by pulverised fuel in channels and pipework of coal-fired power plant. *Powder Technol.* **2002**, *125*, 242–250. [CrossRef]

36. Troiano, M.; Santagata, T.; Montagnaro, F.; Salatino, P.; Solimene, R. Impact experiments of char and ash particles relevant to entrained-flow coal gasifiers. *Fuel* **2017**, *202*, 665–674. [CrossRef]

37. Troiano, M.; Montagnaro, F.; Salatino, P.; Solimene, R. Experimental characterization of particle-wall interaction relevant to entrained-flow gasification of biomass. *Fuel* **2017**, *209*, 674–684. [CrossRef]

38. Troiano, M.; Montagnaro, F.; Solimene, R.; Salatino, P. Modelling entrained-flow slagging gasification of solid fuels with near-wall particle segregation. *Chem. Eng. J.* **2019**, *377*, 119962. [CrossRef]

39. Troiano, M.; Solimene, R.; Montagnaro, F.; Salatino, P. Char/ash deposition and near-wall segregation in slagging entrained-flow gasification of solid fuels: From experiments to closure equations. *Fuel* **2020**, *264*, 116864. [CrossRef]

40. Xie, J.; Dong, M.; Li, S.; Mei, Y.; Shang, Y. An experimental study of fly ash particle oblique impact with stainless surfaces. *J. Aerosol Sci.* **2018**, *123*, 27–38. [CrossRef]

41. Darko, R.; Olivier, S. Modelling of three-dimensional particle rebound from an anisotropic rough wall. *Powder Technol.* **2021**, *393*, 165–183.

42. Wilson, J.; Qiao, R.; Kappes, M.; Loebig, J.; Clarkson, R. The Importance of Shape in Particle Rebound Behaviors. *J. Turbomach.* **2023**, *145*, 041005. [CrossRef]

43. Tukey, J.W. *Exploratory Data Analysis*; Addison-Wesley: Reading, MA, USA; Menlo Park, CA, USA; London, UK; Amsterdam, The Netherlands, 1977.

44. *ISO 5074:2015*; Hard Coal–Determination of Hardgrove Grindability Index. International Organization for Standardization: Geneva, Switzerland, 2015.

45. Williams, O.; Taylor, S.; Lester, E.; Kingman, S.; Giddings, D.; Eastwick, C. Applicability of Mechanical Tests for Biomass Pellet Characterisation for Bioenergy Applications. *Materials* **2018**, *11*, 1329. [CrossRef]

46. Dong, M.; Xie, J.; Bai, L.; Li, S. An Experimental Investigation on the Influence of Temperature on the Normal Impact of Fine Particles with a Plane Surface. *Energies* **2014**, *7*, 2079–2094. [CrossRef]

47. Li, S.; Wu, Y.; Whitty, K.J. Ash Deposition Behavior during Char–Slag Transition under Simulated Gasification Conditions. *Energ. Fuel* **2010**, *24*, 1868–1876. [CrossRef]